TITLE:

A TRANSPARENT WHEEL-BASED PLATFORM FOR LOCOMOTION-ON-DEMAND AND MULTIMODAL BODY AND FACIAL KINEMATICS IN HEAD-FIXED MICE

Authors:

Pratik S Paranjape[1], Tahoura Mohammadi Ghohaki[1], Samsoon Inayat[1,2]

1. Department of Psychology, University of Nevada, Las Vegas, USA
2. Corresponding author: sam.inayat@unlv.edu

ABSTRACT

Understanding how the brain transforms sensory input and internal state into coordinated action requires behavioral paradigms that provide precise, multimodal measurements of movement and arousal while remaining compatible with neural recording techniques. Here we present a modular, low-cost behavioral platform that enables locomotion-on-demand in head-fixed mice using a transparent running wheel combined with air-stream–induced stimulation. This design provides unobstructed visual access to ventral paw movements while simultaneously capturing whole-body kinematics, facial motion, and eye-related signals from multiple camera perspectives. The system integrates Arduino-based stimulus control, high-resolution encoder measurements, Raspberry Pi–based videography, and LED-driven temporal synchronization across independently acquired data streams. Using a proof-of-principle dataset from a single, well-trained animal, we demonstrate that air delivery reliably induces structured locomotion with reproducible trial timing on a transparent wheel. Optical-flow–based motion metrics and DeepLabCut pose estimation reveal robust, stimulus-locked increases in paw, limb, and facial movements during air-on epochs relative to air-off periods. LED-based synchronization enables accurate segmentation of stimulus epochs across video modalities despite differences in sampling rates, with air-on durations showing strong agreement between video-derived and DAQ-recorded measures. Correlation analyses further reveal state-dependent reorganization of coordinated body kinematics during locomotion, indicating structured coupling among limb and whole-body measures rather than a uniform increase in movement. This work establishes a flexible framework for studying stimulus-evoked locomotion and provides a platform well suited for integration with neural imaging and electrophysiology, as well as for future investigations of sensorimotor coordination and behavioral state changes in health and disease.

SIGNIFICANCE STATEMENT

Quantifying how the brain generates coordinated movement requires behavioral paradigms that provide precise, multimodal measurements while remaining compatible with neural recording techniques. We introduce a low-cost, modular behavioral platform that enables locomotion-on-demand in head-fixed mice using a transparent running wheel, allowing simultaneous visualization of ventral paw movements, facial dynamics, and eye-related signals. By combining stimulus-induced locomotion with synchronized multi-camera videography and open-source analysis pipelines, this system overcomes key limitations of existing head-fixed locomotion assays that rely on prolonged reward-based training or provide only limited behavioral readouts.

KEYWORDS

Head-fixed locomotion; stimulus-induced locomotion; behavioral kinematics; transparent running wheel; multimodal videography; optical flow; DeepLabCut; mouse behavior

INTRODUCTION

Coordination and motor control are primary functions of the brain that enable animals to navigate their environment and survive. The motor-control problem solved by the brain is highly complex: movements involve multiple degrees of freedom, and the same action can be achieved through different combinations of muscles [1–3]. This redundancy means that understanding how the brain generates coordinated movement requires precise measurement of behavior at multiple levels, from whole-body and limb kinematics to facial and autonomic indicators of arousal [4–6]. To link these components with neural activity, it is essential to develop advanced experimental setups capable of capturing motor output and internal state with high temporal and spatial precision [7–9] . Developing such comprehensive systems is a critical step toward understanding how distributed neural networks transform perception and motivation into organized action and is the goal of the present study.

Behavioral paradigms have evolved over the past century from early ethological observations to laboratory research employing conditioning boxes, mazes, and sophisticated head-fixed tasks incorporating virtual reality, videography, electrophysiology, and brain imaging [10–13]. Although head fixation involves unnatural restraint, it enables spatially precise imaging of brain structure and activity [14]. Most experimental rigs, however, quantify only limited aspects of behavior, for example belt speed as a proxy for running behavior on a conveyor belt or kinematics of a restricted set of body parts (limbs, whiskers, or eyes), typically using a single video stream, thereby constraining the range of investigative questions that can be addressed [15–17]. Furthermore, many behavioral paradigms rely on extensive reward-based conditioning, in which water-deprived animals receive water as a reward, and training times often span several weeks, limiting throughput and experimental efficiency. Stimulus-induced locomotion paradigms, such as air-stream–based approaches, offer an alternative by evoking locomotion on demand without prolonged conditioning and have been demonstrated primarily using treadmill or

linear conveyor-belt systems [18–21]. However, these approaches have not been systematically implemented or validated using transparent running wheels that would permit unobstructed, multi-angle videography of the animal during locomotion [22,23]. An important gap therefore remains in determining whether stimulus-induced locomotion can be combined with a wheel-based, visually accessible platform to enable simultaneous, high–temporal resolution measurement of whole-body kinematics, facial dynamics, and pupil-based arousal in head-fixed mice [24,25]. Bridging this gap requires integration of behavioral motivation, precise stimulus control, and synchronized multimodal recording within a single experimental framework [26–28].

This study presents a novel behavioral setup that enables locomotion-on-demand with simultaneous measurement of body and facial kinematics together with arousal state in head-fixed mice [29]. The system is low-cost and modular, constructed primarily from readily available components, including Arduino and Raspberry Pi boards, and is accompanied by detailed design schematics, bills of materials, and open-source code for stimulus control, data acquisition, and analyses [30,31]. In contrast to previous methods, our pipeline incorporates an efficient preprocessing approach for videographic data that optimizes performance with DeepLabCut, allowing rapid and accurate pose estimation and tracking of multiple body parts [32]. This integration permits comprehensive analysis of both body and facial kinematics and their relationship to pupil-based arousal during states of immobility and locomotion-in-place [33,34].

ETHICS STATEMENT, EXPERIMENTAL MODEL, AND SUBJECT DETAILS

All animal procedures were performed in compliance with protocols approved by the Institutional Animal Care and Use Committee (IACUC) of the University of Nevada, Las Vegas, and were conducted in accordance with the guidelines for the ethical use of animals established by the National Institutes of Health and relevant institutional regulations. Adult male C57BL/6J-Tg(Thy1-

GCaMP6s)GP4.3Dkim/J mice were used in this study. The example animal shown was ~14 months old at the time of behavioral recordings. Head-fixation surgery was performed at ~13 months of age.

METHODS

Surgery

The procedure was carried out using sterile technique. Animals received a subcutaneous injection of 0.2 mL of a sterile 0.9% saline solution before surgery. Anesthesia was induced and maintained with isoflurane (2–3% for induction; 1–1.5% for maintenance), and the animal was placed on a heating pad. Following induction of anesthesia, the mouse was head-fixed in a stereotaxic (Harvard Apparatus, Inc). A midline incision was made to expose the skull. The skull surface was cleaned and dried, and a custom-designed headplate was positioned and secured to the skull using dental cement (C&B METABOND®, see BOM). The headplate was fabricated from black polyactic acid (PLA) material (Official Creality Hyper PLA Filament 1.75mm, see BOM) using a 3D printer (Creality K1C 3D, see BOM) and designed to provide stable and repeatable head fixation during behavioral experiments.

After implantation, the skin surrounding the headplate was sealed using dental acrylic as needed. Postoperative care included subcutaneous administration of meloxicam (5 mg/kg) for analgesia for 2–3 days following surgery. Animals were allowed to recover fully before habituation to head fixation and subsequent behavioral testing. Behavioral experiments were conducted when the animals were ~14 months old.

Behavioral Setup

Mechanical Hardware

The behavioral apparatus was built on a rigid aluminum base plate (approximately 8 × 12 inches, 0.5-inch thickness), which served as the primary mechanical support for all components. A central hole was

drilled into the base plate to mount a vertical cylindrical aluminum rod, which functioned as the main structural axis of the setup. All major mechanical elements, including the running wheel, head-fixation assembly, camera mounts, and air-delivery components, were attached either to this rod or the base plate using standard laboratory clamps and rods (Fig. 1).

A non-motorized transparent running wheel (Bucatstate Hamster Wheel) was mounted on the vertical rod using the manufacturer provided attachment. For the wheel, the shaft rod itself was fixed, while the wheel rotated freely around it. This configuration allowed unobstructed visual access to the animal from below and the sides while maintaining mechanical stability during locomotion. The entire apparatus was enclosed within a casing constructed from 1/4-inch acrylic sheets, forming a transparent enclosure around the animal to provide physical containment while preserving visibility for videography. A removable silicone tray was placed on the base plate directly beneath the transparent running wheel to collect feces and urine during experiments, facilitating hygiene and rapid cleaning between sessions.

Head fixation was achieved by attaching a custom headplate clamp assembly to the same vertical rod. A rectangular aluminum bar with a square cross-section was mounted using clamps and served as the support for the headplate holder. The headplate holder incorporated two threaded holes to secure the implanted headplate using screws (thread specifications provided in the BOM). This arrangement allowed precise and repeatable positioning of the animal’s head relative to the running wheel and cameras. A 3D printed rigid animal casing was positioned around the head-fixed region of the wheel to restrict lateral movement and prevent the animal from reaching the edges of the running wheel during locomotion.

Multiple cameras were mounted around the apparatus using standard acrylic camera holders supplied with the cameras (see BOM). These holders were secured to rods and clamps attached to the aluminum

base plate, enabling flexible positioning and alignment of cameras for bottom-view, facial, and pupil imaging. All camera mounts and associated hardware are detailed in the BOM.

Wheel position and rotation were monitored using a rotary encoder mounted directly to the running wheel via a custom-designed, 3D-printed fixture. In this configuration, the encoder wheel rotated with the transparent running wheel, while the encoder body was fixed to the stationary horizontal shaft rod. This design enabled accurate measurement of wheel position and speed without interfering with wheel rotation or animal movement. The 3D design files for the encoder mount are provided in the supplementary materials.

Finally, the vertical rod also supported the air-delivery tubing. Pressurized air was supplied from a laboratory wall outlet (~70 PSI) and routed through an inline pressure regulator (see BOM) to reduce the operating pressure to ~10 PSI at the setup. Regulated air was delivered to the animal via flexible tubing connected to a 3 mL syringe mounted on the mechanical frame, which served as a stable and precisely positionable air nozzle. Airflow to the syringe was gated by a solenoid valve placed in-line with the tubing and controlled electronically via a solid-state relay driven by the Arduino (see below). This configuration enabled rapid, reproducible onset and offset of the air stream with minimal mechanical vibration while allowing fine adjustment of both air pressure and nozzle positioning relative to the animal.

Electronic Hardware

The electronic hardware integrates behavioral control, kinematic measurement, and synchronized data acquisition across multiple devices. Locomotion was quantified using a rotary quadrature encoder (Broadcom / Avago 3 Channel 1000CPR, see BOM) mounted to the running wheel, providing two digital quadrature outputs (Channel A and Channel B). These encoder signals were routed in parallel to an Arduino microcontroller (Mega 6250) for real-time behavioral control and to a National Instruments

USB-6259 data acquisition (DAQ) card for high-resolution recording. On the DAQ, encoder signals were acquired using hardware counters and sampled in MATLAB at 5 kHz, allowing precise reconstruction of wheel position and running speed (Fig. 2).

The Arduino continuously monitored the encoder signals to implement distance-based control of the behavioral paradigm (see below). When predefined criteria were met, the Arduino generated a TTL output that drove a solid-state relay, which in turn actuated a solenoid valve controlling the air stream used to induce locomotion. The same air-control TTL signal was also routed to the USB-6259 and recorded at 5 kHz, enabling precise temporal alignment between locomotion, stimulus delivery, and behavioral state. Behavioral execution was gated by dual control inputs: a software-generated TTL signal from the USB-6259 (digital output) and a manual hardware switch. Both signals were required to be high for the behavioral paradigm to run, allowing flexible control and safe manual intervention during experiments. The DAQ-generated TTL control signal was additionally distributed to Raspberry Pi computers via GPIO pin 17. On each Raspberry Pi, custom Python acquisition scripts monitored this GPIO line and initiated video recording only when the trigger signal was high.

Two Raspberry Pi systems were used for videographic acquisition. One Raspberry Pi recorded a single camera providing a ventral (bottom) view of the animal and running wheel, while a second Raspberry Pi controlled two cameras simultaneously for facial and pupil imaging. All cameras, except the pupil camera, were illuminated using infrared (IR) light sources to enable video acquisition in complete darkness, as all training and testing were performed without visible illumination. Camera resolution (1440 x 1080 for bottom and face cameras, 320 x 240 for pupil camera), frame rate (60Hz), and acquisition parameters were configured via custom Python code running on the Raspberry Pi systems. Video recording commenced automatically upon receipt of a TTL trigger signal. When MATLAB-based

acquisition on the USB-6259 was terminated, the trigger signal was driven low, stopping both the behavioral paradigm and video acquisition in a synchronized manner.

Video-to-behavior synchronization was further validated using an LED-based timing marker. A visible red LED mounted within the camera field of view was driven by the same TTL signal that controlled air delivery. As a result, LED illumination provided a direct visual indicator of air onset and offset within the video streams, enabling precise alignment of videographic, behavioral, and kinematic data during offline analysis.

In addition to behavioral and video signals, the USB-6259 received synchronization inputs from the two-photon microscope frame clock, allowing alignment of imaging data with locomotion and stimulus events. The DAQ architecture also permits integration of electrophysiological signals, enabling future multimodal recordings within the same synchronized framework.

Behavioral Paradigm: Air-Induced Running on A Wheel

Animals were habituated to head fixation over three consecutive days. During habituation, mice were head-fixed twice per day, with session durations gradually increased from 5 to 30 minutes to acclimate animals to restraint and the behavioral apparatus. Following habituation, mice were trained to run on the transparent running wheel while head fixed. All movement was generated voluntarily by the animal as the wheel is non-motorized. Training and testing were performed in the absence of visual cues, and the wheel surface was cleaned between sessions.

Locomotion was induced using a mild, continuous air stream directed toward the animal’s back. Air delivery was controlled by a solenoid valve driven by an Arduino-based system and supplied via the building’s compressed air line through a pressure regulator. The air stream served as a movement-inducing stimulus rather than an aversive reinforcer. On each trial, air onset initiated a running epoch during which the animal was required to run a predefined distance on the wheel, measured using the

rotary encoder attached to the wheel. Once the target distance was reached, the air stream was automatically terminated, marking the end of the trial. Trials were separated by an intertrial interval of 15 s [35,36].

Training and testing both were carried out in a dark environment. Training followed a progressive distance schedule. The required running distance initially started at short distances ~5cm and was gradually increased across trials. In the final configuration used for testing, animals were required to run a fixed distance of 25 cm to terminate the air stimulus. If the animal completed the target distance with sufficient and continuous locomotion, the trial was considered successful. Animals were trained until they reliably completed the required distance across the majority of trials within a session. Following training, the same paradigm was used during data collection sessions for behavioral and videographic analysis.

Data Analysis

Behavioral and control signals were analyzed using custom-written scripts in MATLAB (MathWorks). Encoder signals acquired via the USB-6259 were processed to extract wheel position, distance traveled, and running speed for each trial. Behavioral events, including air onset and offset, were aligned to encoder-derived kinematic measures using recorded TTL synchronization signals. In addition to hardware-based TTL synchronization, air onset and offset were independently identified directly from the video recordings using an LED timing marker positioned within the camera field of view. The LED was driven by the same control signal as the air-delivery solenoid, allowing air-related events to be extracted directly from the videos and used for verification and alignment of videographic and behavioral data (see above).

Video data acquired from multiple camera views were analyzed using DeepLabCut, a markerless pose estimation framework based on deep learning. Separate DeepLabCut networks were trained to identify

key body landmarks from each camera view. For the bottom-view camera, the positions of the forepaws and hind paws were tracked to quantify limb kinematics during locomotion. For the facial camera, regions corresponding to the face, whiskers, and nose were identified to extract facial and whisker-related movements. For the eye camera, pupil boundaries were detected and used to estimate pupil diameter as a measure of arousal state.

Video preprocessing, pose estimation, and post-processing were performed using a combination of DeepLabCut utilities and custom MATLAB and Python scripts. Kinematic and pupil-derived measures were synchronized with encoder and stimulus signals using shared timing markers, enabling trial-by-trial alignment of locomotion, facial dynamics, and arousal-related variables. All analysis scripts will be made publicly available to facilitate replication and reuse of the analysis pipeline.

Video preprocessing

To reduce storage requirements and accelerate downstream computer-vision processing, the paws and face videos were downsampled in spatial resolution prior to analysis. Videos were resized to 25% of their original width and height (i.e., 1/4 scaling in each dimension) using OpenCV with area-based interpolation (INTER_AREA), which is well-suited for high-quality downscaling. The pupil video was recorded at a smaller native resolution and was not resized. Resized videos were saved alongside the originals with a "_reduced" suffix to preserve provenance.

ROI selection and metadata

For each video modality (paws, face, pupil), a rectangular region of interest (ROI) was selected manually on the first frame using an OpenCV interactive ROI tool. The ROI coordinates (x, y, width, height) and the source video path were saved to a sidecar JSON file (e.g., "*_roi.json"). This ensured that the same ROI definition could be reused for reprocessing, parameter tuning, and reproducible analysis across sessions.

Optical flow and motion-energy extraction

To obtain a fast, model-free characterization of movement dynamics without requiring pose-estimation networks, we computed dense optical flow within each ROI using the Dual TV-L1 method implemented in OpenCV (opencv-contrib). For each frame pair, the video was cropped to the ROI, converted to grayscale, and optical flow was estimated between successive frames. As summary motion features, we computed the mean horizontal and vertical flow components (avg_u, avg_v) within the ROI. In parallel, we computed a complementary motion-energy measure as the mean absolute frame-to-frame intensity difference within the ROI. For each modality, outputs were written to a CSV file containing frame index, timestamp (ms; from the video container), average flow components, and motion-energy values (e.g., "*_OF.csv"). Processing was performed offline.

Statistical Analyses

Statistical analyses were performed using MATLAB (MathWorks). Because the experiments presented here were designed as proof-of-principle demonstrations using data from a single animal ($n = 1$), statistical tests were applied for exploratory, within-session comparisons rather than for population-level inference. For each trial, behavioral measures such as running speed were quantified separately during air-on and the immediately preceding air-off epochs. Trial-averaged values were then compared between conditions using paired, two-tailed t-tests. In addition, distributions of speed values during air-on and air-off periods were compared using the Kolmogorov–Smirnov test. Statistical significance was assessed at a threshold of $p < 0.05$. Data are reported as mean ± standard deviation unless otherwise stated.

RESULTS

Air-induced locomotion produces reliable trial structure on a transparent wheel

To determine whether air-stream–induced locomotion generates reliable and repeatable trial structure on a transparent running wheel, we first examined the relationship between air delivery and locomotor behavior in a head-fixed mouse. Continuous wheel-derived speed measurements revealed robust, stimulus-locked increases in running during air application, followed by rapid decreases in speed upon air offset (Fig. 2A). Over an ~11-minute recording session, the animal completed 34 trials in which air onset consistently triggered locomotion and air offset marked transitions to lower-speed states. In each trial, air delivery was maintained until the animal completed a fixed running distance of 25 cm, thereby defining discrete air-on and air-off epochs.

To quantify the separation between locomotor states, we compared the distributions of running speed during air-on and air-off periods. Cumulative speed distributions showed a pronounced rightward shift during air-on epochs relative to air-off epochs (Fig. 2B), indicating robust modulation of locomotion by the air stimulus (Kolmogorov–Smirnov test, ***$p < 0.001$).

Next, we aligned running speed to stimulus transitions to assess temporal dynamics across trials. Following air onset, running speed increased rapidly and reached a stable plateau within approximately 1–2 seconds (Fig. 2C). Conversely, air offset was followed by a gradual decay in running speed, reflecting controlled disengagement from locomotion rather than abrupt stopping (Fig. 2D). These aligned averages demonstrate consistent temporal structure across trials despite natural variability in instantaneous speed.

Finally, to assess trial-to-trial reliability, mean running speed was computed for each air-on trial and compared with the immediately preceding air-off period. Across 34 trials, average speed during air-on epochs was significantly higher than during air-off epochs (paired t-test, ***$p < 0.001$; Fig. 2E). These

results demonstrate that air-induced locomotion on a transparent wheel produces reliable, repeatable trial structure suitable for quantitative behavioral and multimodal analyses, even at the level of a single-animal proof-of-principle demonstration.

LED-based synchronization enables alignment of air stimulus across video streams

LED-based synchronization enabled alignment of the air stimulus across independently acquired video streams. To synchronize the air stimulus across video streams, we leveraged a red LED that was directly driven by the same control signal as the air solenoid. The LED was positioned within the field of view of each camera (paws, face, and pupil), allowing air-on and air-off events to be detected directly from the video data. LED intensity signals were extracted independently from each video stream and converted into binarized air-state vectors using a data-driven single-threshold approach. Air-on and air-off epochs were then identified from rising and falling transitions in the binarized LED signal, yielding independent estimates of air delivery timing for each modality. Visual inspection of LED-aligned frame montages revealed consistent detection of air onset across all three video views, with frame-by-frame transitions occurring within the expected temporal resolution imposed by the video sampling rate (60 Hz; Fig. 3A). When plotted over the full recording session, the binarized air-state signals from the paws, face, and pupil videos exhibited highly similar trial structure, although small offsets in absolute timing were apparent between streams (Fig. 3B). These offsets reflect independent camera clocks and do not indicate loss of stimulus information.

To quantify synchronization accuracy, air-on and air-off durations extracted from LED-derived signals in each video stream were compared against durations measured from the DAQ-recorded air-control signal (5 kHz sampling), which served as the temporal reference. Trial-by-trial comparisons revealed strong correspondence between video-derived and DAQ-derived measures across all modalities (Fig.

3C). In particular, air-on durations showed excellent agreement, with high correlations between LED-derived and DAQ-derived values (paws: r = 0.991; face: r = 0.985; pupil: r = 1.000; N = 34 trials). Mean air-on timing errors were small (|mean| < 200 ms) and were consistent with the temporal discretization imposed by the video frame rate (60 Hz). Air-off durations exhibited larger variability and weaker correlations with DAQ measures. This increased variance reflects the fact that air termination was behavior-dependent (occurring upon completion of a target running distance) rather than being triggered by a fixed-duration command. Importantly, these deviations were small relative to the total air-off interval (~15 s) and therefore do not limit within-epoch analyses of behavior, kinematics, or arousal. Together, these results demonstrate that LED-based synchronization provides a robust and modality-independent method for segmenting air-on and air-off periods across multiple video streams. While small timing mismatches in absolute onset and offset times are unavoidable due to independent acquisition clocks, air-state durations are preserved with sufficient precision for within-epoch behavioral, kinematic, and arousal analyses.

Air-induced locomotion produces reliable paw kinematics on a transparent wheel

To determine whether air-stream–induced locomotion yields reliable and quantifiable limb kinematics on a transparent wheel, we first examined whole-body and paw-specific movement using complementary video-based analyses. Optical-flow and motion-energy metrics extracted from a paw-view video revealed robust, stimulus-locked increases in movement during air application (Fig. 4). Paw optical-flow–derived speed and motion energy increased rapidly following air onset and decreased following air offset, producing well-defined air-on and air-off epochs across repeated trials (Fig. 4B–D). Trial-averaged analyses aligned to air onset and offset showed consistent temporal structure, with a

rapid rise in paw movement following air onset and a gradual decay following air termination (Fig. 4C,D).

Across trials (n = 34), mean paw speed during air-on epochs was significantly higher than during air-off epochs (paired t-test, $p < 0.001$; Fig. 4E), as was motion energy ($p < 0.001$; Fig. 4F). These results demonstrate that air delivery reliably evokes reproducible paw and body movement on the transparent wheel, providing a robust behavioral readout that is temporally aligned to the stimulus.

To further resolve limb-specific kinematics, we applied DeepLabCut-based pose estimation to track individual body points, including all four paws, tail base, and nose (Fig. 5). Tracking confidence was high across all body parts, with the majority of frames exceeding a likelihood threshold of 0.9 and sharply peaked likelihood distributions (Fig. 5B), indicating stable and reliable pose estimation throughout the session. Time-resolved trajectories of tracked points revealed structured, stimulus-locked changes in both horizontal and vertical paw positions during air-on epochs (Fig. 5C), consistent with coordinated locomotor behavior rather than sporadic or noisy movement.

Quantifying per-trial movement speeds for each tracked body point showed that all paws, as well as the tail base and nose, exhibited significantly higher speeds during air-on periods compared to pre-air-off intervals (paired t-tests, all $p < 0.001$; Fig. 5D). The consistent increase across multiple body points confirms that air-induced locomotion on the transparent wheel engages coordinated whole-body movement rather than isolated limb motion.

These analyses demonstrate that air-stream stimulation produces reliable, repeatable, and quantifiable paw and body kinematics in head-fixed mice running on a transparent wheel. The combination of optical-flow–based measures and markerless pose estimation provides complementary, scalable approaches for capturing locomotor dynamics, establishing this platform as a robust foundation for multimodal behavioral and neural analyses.

Facial and Eye dynamics during air-induced locomotion

To assess stimulus-locked facial movements and autonomic correlates during air-induced locomotion, we analyzed front-facial and side-facial video streams acquired simultaneously with paw kinematics (Figs. 6 and 7). Optical-flow (OF) and motion-energy measures were extracted from predefined facial regions of interest to quantify gross facial motion, while DeepLabCut (DLC) was used to track discrete facial landmarks to evaluate tracking reliability and movement consistency.

In the front-facial view, air delivery produced a clear and reproducible increase in facial motion. Time-resolved OF-derived facial speed and motion energy closely tracked air-on epochs identified from the LED signal (Fig. 6B). Trial-aligned analyses revealed a rapid increase in facial motion following air onset (Fig. 6C) and a gradual decay following air offset (Fig. 6D). Across trials, mean facial OF speed and motion energy were significantly higher during air-on compared to air-off epochs (paired t-tests, ***$p < 0.001$; Fig. 6E–F), indicating robust stimulus-locked facial activation during locomotion.

DLC tracking of facial landmarks (nose, nostrils, mouth, and snout-side points) showed high reliability across recordings, with a large majority of frames exceeding a likelihood threshold of 0.9 and steep cumulative likelihood distributions (Fig. 6H). Although whisker landmarks were included in the initial DLC model, whisker tracking was inconsistent under the present recording conditions and analysis parameters. Whisker kinematics were therefore not interpreted further in this study, but the reliability of non-whisker facial landmarks demonstrates the feasibility of detailed facial tracking in this preparation.

Side-facial recordings provided complementary measurements of facial motion and eye dynamics (Fig. 7). As in the front-facial view, OF-derived facial speed and motion energy increased reliably during air-on epochs (Fig. 7B–F), confirming that air delivery evokes coordinated facial movement across viewing angles. In contrast, analysis of the eye region revealed no systematic modulation of eye or pupil area associated with air delivery (Fig. 7G–H). Experiments were conducted in darkness using infrared

illumination, resulting in a maximally dilated pupil throughout the session. Under these conditions, neither air delivery nor the red LED used to indicate air onset produced detectable changes in eye or pupil area, indicating an absence of measurable autonomic pupil responses in this context.

These results demonstrate that air-induced locomotion is accompanied by robust, stimulus-locked facial movements that can be quantified using both optical-flow–based measures and markerless pose tracking. At the same time, the absence of pupil modulation under dark conditions establishes a useful baseline for interpreting future autonomic measurements obtained under different lighting or task contingencies.

State-dependent reorganization of coordinated body kinematics

To examine how air-induced locomotion alters coordination across behavioral and kinematic modalities, we computed trial-mean correlation matrices across paw, facial, limb, and eye-related measures separately for air-off and air-on epochs (Fig. 8); 5 s before and 5 s after air onset. During air-off periods, correlations were broadly high and relatively uniform across measures, reflecting a low-movement regime in which residual motion and measurement noise contributed similarly across modalities (Fig. 8A). In this state, limb speeds, facial motion, and paw-based optical-flow measures showed strong mutual correlations, consistent with a globally quiescent behavioral baseline.

In contrast, air-on epochs revealed a marked reorganization of inter-measure relationships (Fig. 8B). Correlations became more structured and heterogeneous, with strengthened coupling among limb-specific kinematic measures and reduced correlations between limb motion and facial or eye-related signals. This pattern indicates a transition from a globally correlated low-activity state to a behaviorally organized locomotor state in which different body components contribute distinct and coordinated roles. Direct comparison of air-on and air-off correlation matrices (ΔR = air-on − air-off) further highlighted this state-dependent reorganization (Fig. 8C). Air-induced locomotion was associated with selective

increases in correlations among limb speeds and paw-based kinematic measures, alongside decreases in correlations involving facial and eye-region signals. These changes were not uniform across all measures, demonstrating that air-on epochs are characterized by a redistribution of coordination structure rather than a simple scaling of movement magnitude.

Together, these results show that air-induced locomotion drives a systematic reconfiguration of whole-body kinematic coordination across limbs and facial domains. This coordinated reorganization supports the use of the AIR task as a structured behavioral paradigm for probing state-dependent sensorimotor and physiological dynamics across multiple modalities.

DISCUSSION

The primary goal of this study was to develop and validate a modular, low-cost behavioral platform that enables locomotion on demand in head-fixed mice while providing synchronized, multimodal readouts of behavior, kinematics, and autonomic state. A central technical innovation of the platform is the use of a transparent running wheel (with the air-induced running task), which permits unobstructed videographic access to the ventral body surface and limbs during locomotion. This design enables simultaneous measurement of whole-body kinematics, paw dynamics, facial motion, and eye-related signals within a single experimental configuration, without requiring repositioning of the animal or cameras[12,21,24]. Additional methodological novelties include stimulus-induced control of locomotion using air delivery, LED-based temporal synchronization across independent video streams, and the integration of optical-flow–based motion metrics with pose-estimation approaches[35,36]. Importantly, the results presented here are intended as a technical proof of principle rather than a population-level characterization of behavioral or neural phenomena. Accordingly, all analyses were performed on data obtained from a single, well-trained animal (n = 1), allowing focused evaluation of system feasibility,

reliability, temporal precision, and cross-modal synchronization without confounds introduced by inter-animal variability. By establishing stable and reproducible performance at the single-subject level, the present work provides a robust foundation for future studies employing larger cohorts, formal statistical inference, and simultaneous neural recordings.

A key conceptual contribution of this platform is the integration of stimulus-induced locomotion with simultaneous, multi-perspective behavioral readout under head fixation[13,14,23,34,37]. The transparent wheel preserves naturalistic cyclic stepping while enabling direct visualization and quantification of ventral paw kinematics, a combination that is difficult to achieve with opaque or belt-based running systems[6,22]. When combined with synchronized facial and eye videography, this configuration allows concurrent assessment of locomotor output, facial dynamics, and arousal-related signals within the same trials, using a single unified stimulus paradigm[25,26,34]. Notably, locomotion in this system is elicited on demand via a controlled air stream rather than through prolonged reward-based conditioning, substantially reducing training time while maintaining reliable trial structure[36]. Together, these design choices establish a flexible and extensible framework for studying how sensory inputs are transformed into coordinated motor actions and associated behavioral states, while maintaining precise temporal alignment across multiple data streams.

An important advantage of the AIR task is that it provides a rapid, repeatable, and minimally structured means of inducing locomotion without reliance on reward learning, deprivation, or extended shaping procedures. Air-induced locomotion exploits an innate sensorimotor response that can be established reliably within a few sessions, producing behavior with well-defined onset and offset transitions. This structure enables precise segmentation of immobility-to-locomotion and locomotion-to-immobility epochs, which is particularly advantageous for studying state transitions, motor initiation, and context-dependent modulation of neural and behavioral variables[35]. Moreover, because air termination is

behavior-dependent rather than fixed in duration, the paradigm naturally couples stimulus delivery to performance, allowing flexible manipulation of task demands (e.g., target distance or effort) without altering the underlying control logic. These features position the AIR task as a complementary alternative to reward-based locomotion assays, particularly for experiments focused on temporal dynamics and multimodal state changes.

A central design objective of the AIR task was to achieve precise temporal alignment between stimulus delivery and multimodal behavioral measurements acquired across heterogeneous hardware and sampling rates. By combining Arduino-controlled air delivery with LED-based visual markers embedded directly within each video stream, the system provides a robust and redundant synchronization strategy that does not rely on shared clocks or post hoc assumptions about timing. Quantitative comparison of air-on and air-off durations extracted from LED-derived signals against DAQ-recorded air-control signals demonstrated high agreement across video modalities, with deviations largely attributable to the temporal discretization imposed by video frame rates. Importantly, these discrepancies were small relative to the duration of air-on and air-off epochs and do not constrain within-epoch analyses of locomotion, kinematics, or facial dynamics. This synchronization approach ensures reliable stimulus alignment even when video and neural recordings operate at different sampling frequencies, a common challenge in multimodal experimental designs.

Several limitations of the present implementation should be noted. First, although facial and whisker motion could be detected during air delivery, a portion of this movement may reflect direct mechanical effects of the air stream rather than exclusively self-generated behavior. Whiskers, in particular, are lightweight structures that are susceptible to passive deflection, which may contribute to variability in whisker-related measures. This limitation is technical rather than conceptual and can be mitigated in future implementations by incorporating a simple air shield or baffle positioned to protect the face and

whisker pad while preserving airflow to the body. Such shielding would allow clearer dissociation of mechanically induced motion from active sensorimotor whisking. Second, because the running surface is smooth and transparent, transient reductions in traction could in principle occur if moisture accumulates on the wheel surface (e.g., due to urination). In practice, this issue was not observed in the present study, as the animal was well habituated to the head-fixed setup and task demands. Nevertheless, this consideration highlights the importance of adequate habituation and training, as well as routine inspection and cleaning of the running surface, particularly for extended sessions or high-throughput experiments.

The platform described here is readily extensible to a wide range of experimental applications. Future studies will incorporate larger cohorts to enable population-level inference and to assess inter-animal variability in locomotor, facial, and autonomic responses. Critically, the system is designed to integrate seamlessly with simultaneous neural recordings, including two-photon calcium imaging, electrophysiology, and fiber photometry, enabling direct investigation of how neural activity across cortical and subcortical circuits relates to stimulus-evoked locomotion and behavioral state transitions. The modular design further allows straightforward adaptation of task parameters, such as varying air intensity, target distance, or sensory context, to probe graded motor effort, motivation, and sensorimotor integration. Beyond basic motor control, this framework is well suited for studying early alterations in movement, arousal, and coordination in disease models, including aging and neurodegenerative disorders, where subtle behavioral changes may precede overt impairments.

RESOURCE AVAILABILITY

A complete bill of materials (BOM), detailed design schematics, and 3D-printable files for all custom components used in this setup will be provided. All designs, hardware specifications, and associated

software will be made freely available to facilitate replication and adaptation of the system by other laboratories upon acceptance of the manuscript.

Lead contact

Further information and requests for resources and reagents should be directed to and will be fulfilled by the lead contact, Samsoon Inayat (sam.inayat@unlv.edu).

Materials availability

This study did not generate new unique reagents.

Data and code availability

All data and codes used for analyzing data in this paper will be made available upon the acceptance of the manuscript.

AUTHOR CONTRIBUTIONS

All authors contributed to the design of the study. P.P. and S.I. led the design and integration of the behavioral apparatus. P.P. designed and fabricated the 3D-printed components. T.M.G. participated in system integration and performed the animal surgery. T.M.G., P.P., and S.I. conducted the behavioral experiments. P.P. and S.I. developed the Arduino, Raspberry Pi, and MATLAB code for stimulus control, data acquisition, and synchronization. P.P. and S.I. implemented the synchronization and alignment analyses. P.P. and T.M.G. performed the DeepLabCut-based pose estimation analyses. S.I. performed the optical-flow–based motion analyses and wrote the first draft of the manuscript. All authors reviewed and approved the final manuscript.

ACKNOWLEDGEMENTS

We thank the animal care staff at the University of Nevada, Las Vegas for their support and assistance with animal husbandry.

FUNDING

This work was supported by an Interdisciplinary Neuroscience Graduate Assistantship to Pratik Paranjape, Department of Psychology Graduate Assistantship to Tahoura Mohammadi Ghohaki, and internal UNLV funding to Samsoon Inayat.

DECLARATION OF INTERESTS

The authors declare that an invention disclosure related to the behavioral setup described in this manuscript has been filed with the University of Nevada, Las Vegas.

REFERENCES

1. Becker, M. I., Calame, D. J., Wrobel, J. & Person, A. L. Online control of reach accuracy in mice. *Journal of Neurophysiology* **124**, 1637–1655 (2020).
2. Yue, Y. *et al.* Motor training improves coordination and anxiety in symptomatic Mecp2-null mice despite impaired functional connectivity within the motor circuit. *SCIENCE ADVANCES* (2021).
3. Luong, T. N., Carlisle, H. J., Southwell, A. & Patterson, P. H. Assessment of Motor Balance and Coordination in Mice using the Balance Beam. *JoVE* 2376 (2011) doi:10.3791/2376.
4. Heindorf, M., Arber, S. & Keller, G. B. Mouse Motor Cortex Coordinates the Behavioral Response to Unpredicted Sensory Feedback. *Neuron* **99**, 1040-1054.e5 (2018).
5. Nguyen, K. P., Sharma, A., Gil-Silva, M., Gittis, A. H. & Chase, S. M. Distinct Kinematic Adjustments over Multiple Timescales Accompany Locomotor Skill Development in Mice. *Neuroscience* **466**, 260–272 (2021).
6. Vinck, M., Batista-Brito, R., Knoblich, U. & Cardin, J. A. Arousal and Locomotion Make Distinct Contributions to Cortical Activity Patterns and Visual Encoding. *Neuron* **86**, 740–754 (2015).
7. Sun, G. *et al.* Neural representation of self-initiated locomotion in the secondary motor cortex of mice across different environmental contexts. *Commun Biol* **8**, 725 (2025).
8. Quarta, E. *et al.* Distributed and Localized Dynamics Emerge in the Mouse Neocortex during Reach-to-Grasp Behavior. *J. Neurosci.* **42**, 777–788 (2022).
9. Currie, S. P. *et al.* Movement-specific signaling is differentially distributed across motor cortex layer 5 projection neuron classes. *Cell Reports* **39**, 110801 (2022).
10. Carlsen, E. M. M., Nedergaard, M. & Rasmussen, R. N. Versatile treadmill system for measuring locomotion and neural activity in head-fixed mice. *STAR Protocols* **3**, 101701 (2022).

11. Juczewski, K., Koussa, J. A., Kesner, A. J., Lee, J. O. & Lovinger, D. M. Stress and behavioral correlates in the head-fixed method: stress measurements, habituation dynamics, locomotion, and motor-skill learning in mice. *Sci Rep* **10**, 12245 (2020).
12. Warren, R. A. *et al.* A rapid whisker-based decision underlying skilled locomotion in mice. *eLife* **10**, e63596 (2021).
13. Krishnan, S. *et al.* A contextual fear conditioning paradigm in head-fixed mice exploring virtual reality. *eLife* **14**, RP105422 (2025).
14. Giovannucci, A. *et al.* Automated gesture tracking in head-fixed mice. *Journal of Neuroscience Methods* **300**, 184–195 (2018).
15. Niell, C. M. & Stryker, M. P. Modulation of Visual Responses by Behavioral State in Mouse Visual Cortex. *Neuron* **65**, 472–479 (2010).
16. Clack, N. G. *et al.* Automated Tracking of Whiskers in Videos of Head Fixed Rodents. *PLoS Comput Biol* **8**, e1002591 (2012).
17. Bushnell, M., Umino, Y. & Solessio, E. A system to measure the pupil response to steady lights in freely behaving mice. *Journal of Neuroscience Methods* **273**, 74–85 (2016).
18. Jordan, J. T., McDermott, K. D., Frechou, M. A., Shtrahman, M. & Gonçalves, J. T. Treadmill-based task for assessing spatial memory in head-fixed mice. *STAR Protocols* **2**, 100770 (2021).
19. Savier, E. L., Chen, H. & Cang, J. Effects of Locomotion on Visual Responses in the Mouse Superior Colliculus. *J. Neurosci.* **39**, 9360–9368 (2019).
20. Aydın, Ç., Couto, J., Giugliano, M., Farrow, K. & Bonin, V. Locomotion modulates specific functional cell types in the mouse visual thalamus. *Nat Commun* **9**, 4882 (2018).
21. Ignatowska-Jankowska, B. M. *et al.* Accurate Tracking of Locomotory Kinematics in Mice Moving Freely in Three-Dimensional Environments. *eNeuro* **12**, ENEURO.0045-25.2025 (2025).

22. Novak, C. M., Burghardt, P. R. & Levine, J. A. The use of a running wheel to measure activity in rodents: Relationship to energy balance, general activity, and reward. *Neuroscience & Biobehavioral Reviews* **36**, 1001–1014 (2012).
23. Forys, B. J., Xiao, D., Gupta, P. & Murphy, T. H. Real-Time Selective Markerless Tracking of Forepaws of Head Fixed Mice Using Deep Neural Networks. *eNeuro* **7**, ENEURO.0096-20.2020 (2020).
24. Yamada, K. & Toda, K. Pupillary dynamics of mice performing a Pavlovian delay conditioning task reflect reward-predictive signals. *Front. Syst. Neurosci.* **16**, 1045764 (2022).
25. Turner, K. L., Gheres, K. W. & Drew, P. J. Relating Pupil Diameter and Blinking to Cortical Activity and Hemodynamics across Arousal States. *J. Neurosci.* **43**, 949–964 (2023).
26. Sofroniew, N. J., Cohen, J. D., Lee, A. K. & Svoboda, K. Natural Whisker-Guided Behavior by Head-Fixed Mice in Tactile Virtual Reality. *J. Neurosci.* **34**, 9537–9550 (2014).
27. Saleem, A. B., Ayaz, A., Jeffery, K. J., Harris, K. D. & Carandini, M. Integration of visual motion and locomotion in mouse visual cortex. *Nat Neurosci* **16**, 1864–1869 (2013).
28. Stringer, C. *et al.* Spontaneous behaviors drive multidimensional, brainwide activity. *Science* **364**, eaav7893 (2019).
29. The International Brain Laboratory *et al.* Standardized and reproducible measurement of decision-making in mice. *eLife* **10**, e63711 (2021).
30. Petty, G. H. & Bruno, R. M. Attentional modulation of secondary somatosensory and visual thalamus of mice. *eLife* **13**, RP97188 (2024).
31. Whiteway, M. R. *et al.* Partitioning variability in animal behavioral videos using semi-supervised variational autoencoders. *PLoS Comput Biol* **17**, e1009439 (2021).

32. Schweihoff, J. F. *et al.* DeepLabStream enables closed-loop behavioral experiments using deep learning-based markerless, real-time posture detection. *Commun Biol* **4**, 130 (2021).
33. Zhang, Q., Turner, K. L., Gheres, K. W., Hossain, M. S. & Drew, P. J. Behavioral and physiological monitoring for awake neurovascular coupling experiments: a how-to guide. *Neurophoton.* **9**, (2022).
34. Bergmann, R. *et al.* Coordination between Eye Movement and Whisking in Head-Fixed Mice Navigating a Plus Maze. *eNeuro* **9**, ENEURO.0089-22.2022 (2022).
35. Inayat, S., McAllister, B. B., Whishaw, I. Q. & Mohajerani, M. H. DISTINCT NEURAL SIGNATURES OF HIPPOCAMPAL POPULATION DYNAMICS DURING LOCOMOTION-IN-PLACE. (2025).
36. Inayat, S., McAllister, B. B., Whishaw, I. Q. & Mohajerani, M. H. Hippocampal conjunctive and complementary CA1 populations relate sensory events to movement. *iScience* **26**, 106481 (2023).
37. Kobayashi, G. Pupil Dynamics-derived Sleep Stage Classification of a Head-fixed Mouse Using a Recurrent Neural Network.

FIGURES

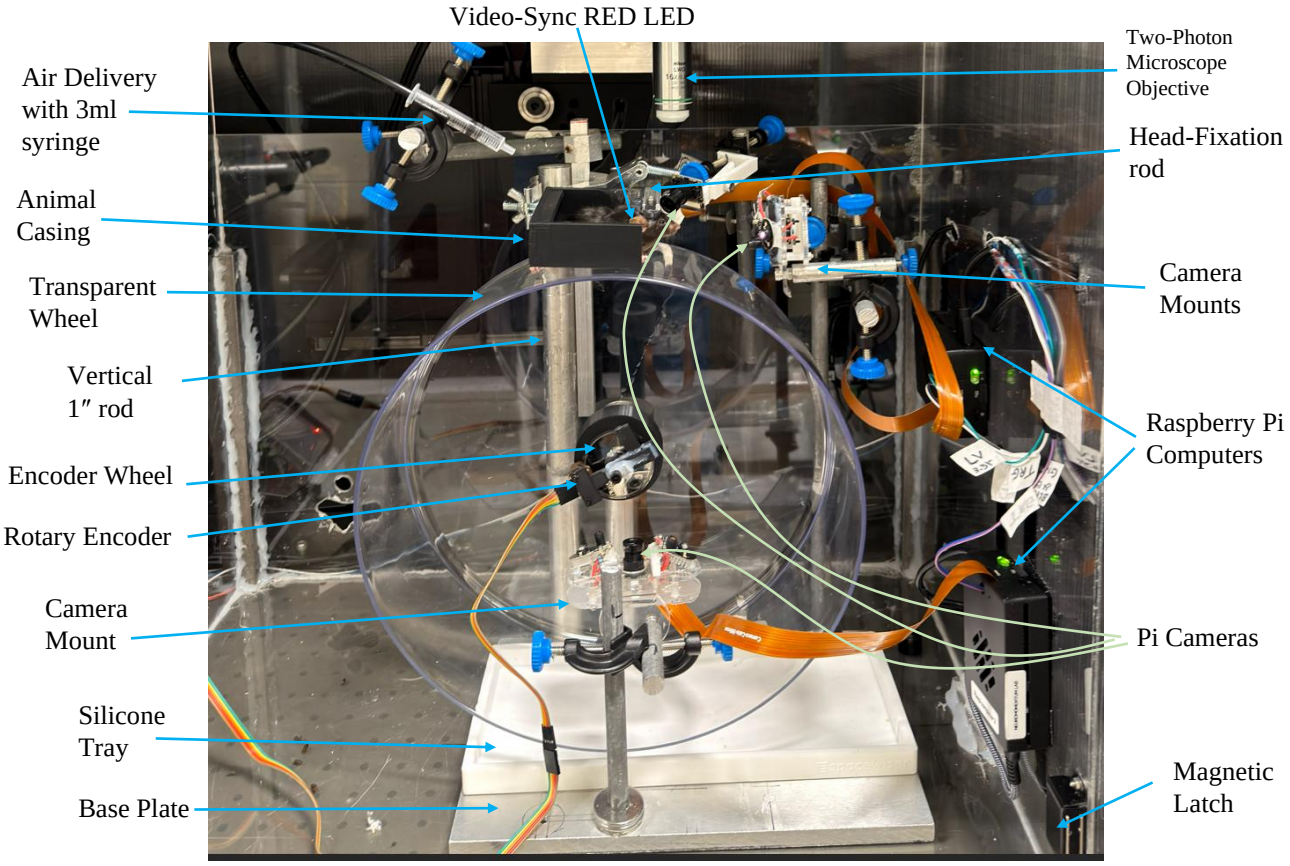
Video-Sync RED LED
Two-Photon Microscope Objective
Air Delivery with 3ml syringe
Head-Fixation rod
Animal Casing
Camera Mounts
Transparent Wheel
Vertical 1″ rod
Raspberry Pi Computers
Encoder Wheel
Rotary Encoder
Camera Mount
Pi Cameras
Silicone Tray
Magnetic Latch
Base Plate

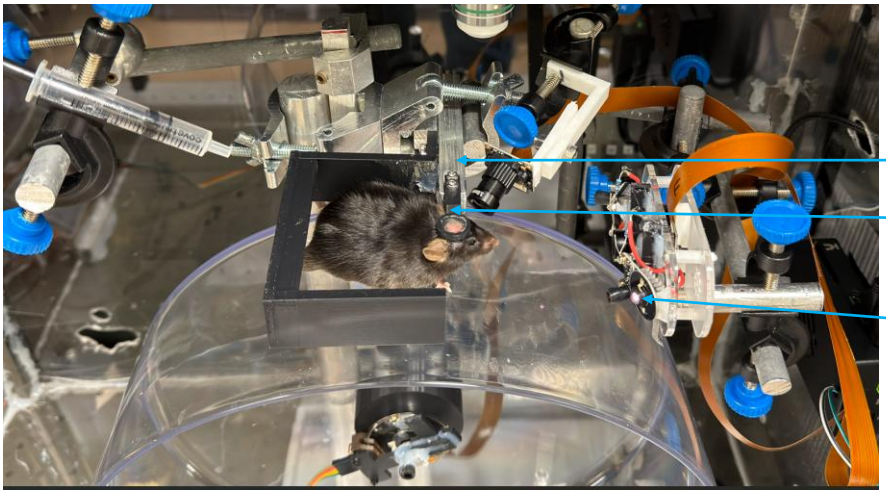
Head-Fixation rod
Head-Plate
Infrared Lights

Figure 1. Overview of the Behavioral Apparatus.

Photographs of the behavioral setup illustrating the major mechanical and electronic components. The system is built around a rigid aluminum base plate supporting a vertical cylindrical rod that serves as the primary structural axis. A transparent running wheel is mounted on the rod and instrumented with a rotary encoder for measurement of wheel position and speed. A removable silicone tray positioned beneath the wheel collects feces and urine during experiments. The animal is head-fixed using a custom headplate clamp attached to the vertical rod. Air delivery is achieved via a syringe-based nozzle positioned above the animal's back. Multiple cameras are mounted around the apparatus for bottom-view, facial, and pupil imaging and are connected to Raspberry Pi computers for synchronized video acquisition. The entire setup is compatible with integration under a two-photon microscope objective for future neural imaging experiments.

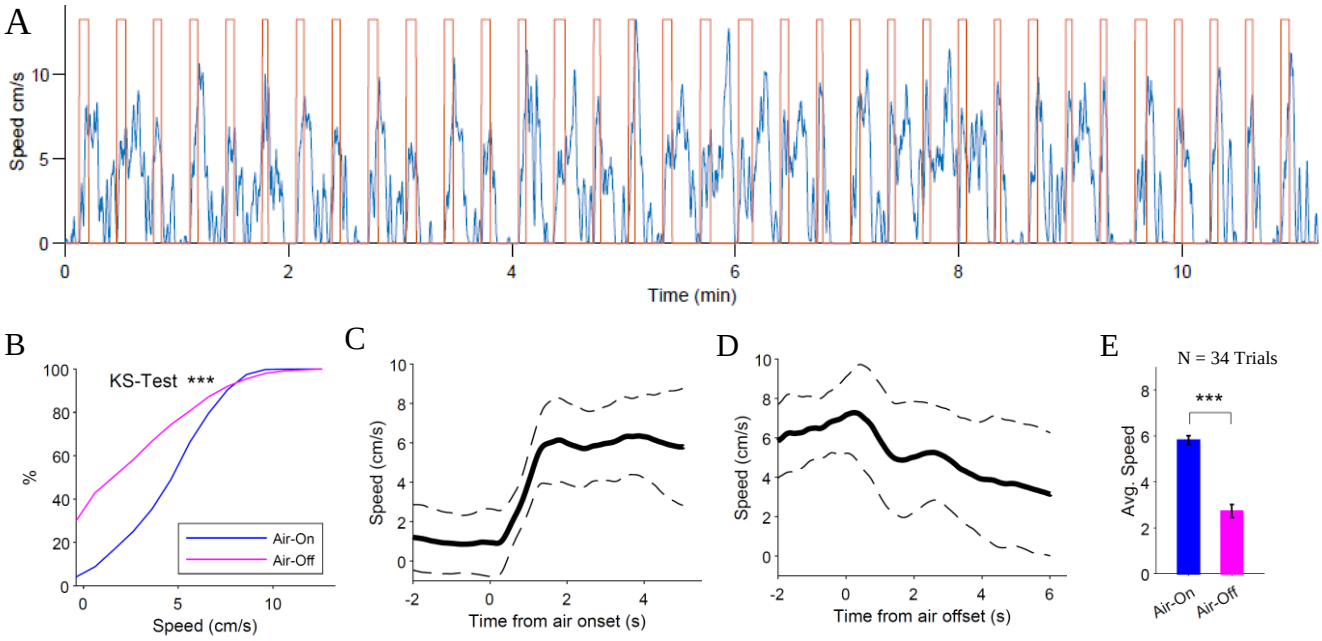

Figure 2. Air-induced locomotion produces reliable and trial-structured running behavior on a transparent wheel.

(A) Continuous recording of wheel-derived running speed (blue) and air stimulus timing (orange) during an example ~11-minute session comprising 34 trials. Air application reliably elicited increases in running speed, which decreased following air offset. **(B)** Cumulative distributions of running speed during air-on (blue) and air-off (magenta) periods across the session. The distributions were significantly different (Kolmogorov–Smirnov test, *** $p < 0.001$), indicating a clear separation between locomotor states. **(C)** Trial-aligned running speed relative to air onset (time 0 s). Solid line indicates the mean speed across trials; dashed lines indicate ±1 standard deviation. Running speed increased rapidly following air onset and reached a stable plateau during air application. **(D)** Trial-aligned running speed relative to air offset (time 0 s). Termination of the air stimulus was followed by a gradual reduction in running speed, demonstrating precise stimulus-locked control of locomotion. **(E)** Mean running speed computed on a per-trial basis during air-on and the immediately preceding air-off periods (N = 34 trials).

Speeds were significantly higher during air-on epochs compared with air-off epochs (paired t-test, *** $p < 0.001$).

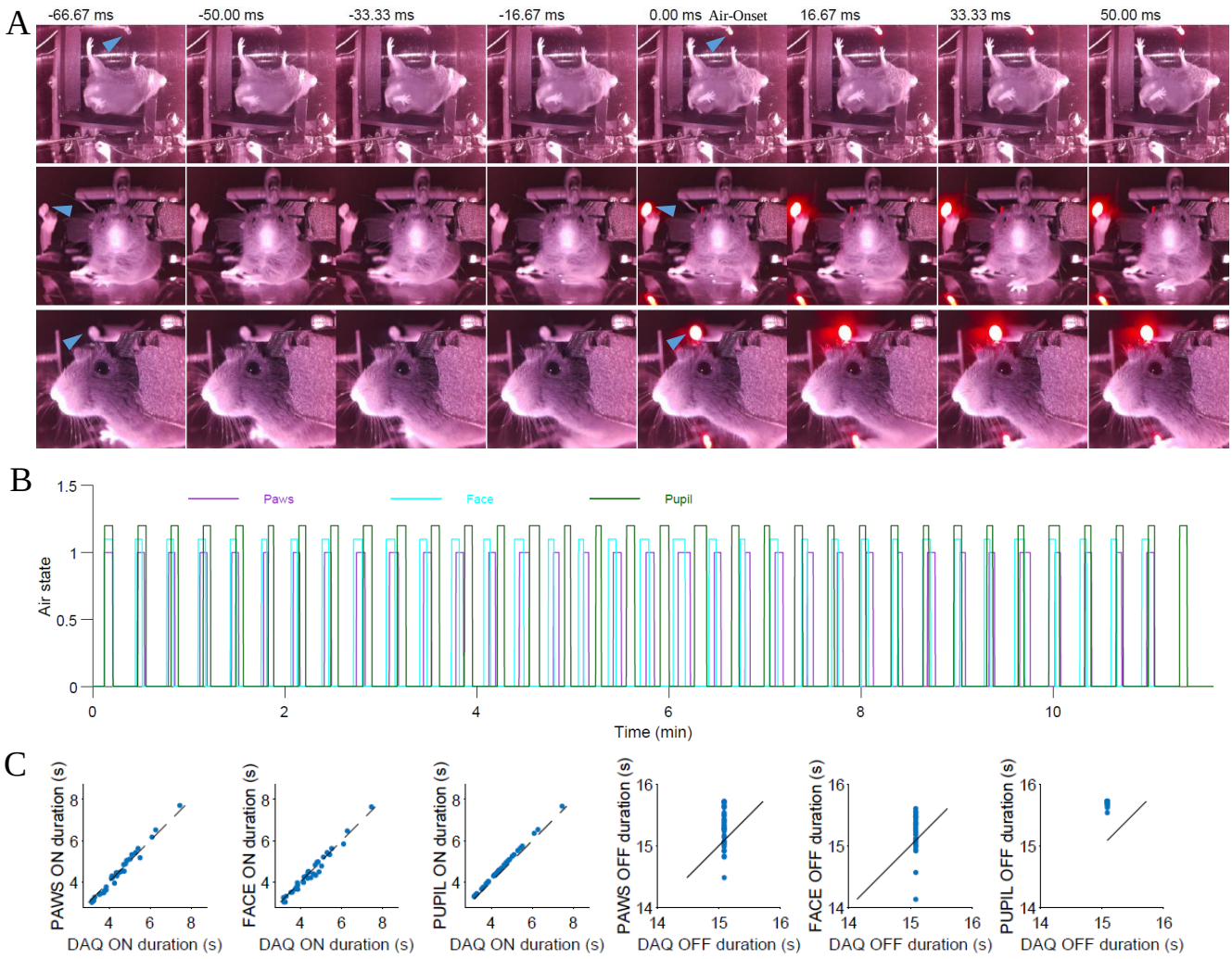

Figure 3. LED-based synchronization enables reliable alignment of air stimulus across behavioral and video modalities.

(A) Representative montages from the three simultaneously acquired video streams (top: paws/bottom view; middle: face/front view; bottom: pupil/side view) aligned to the first detected air-onset event in each video using the LED signal visible in the frame. Frames are shown from −66.7 ms to +50.0 ms relative to air onset (60 Hz sampling). Cyan arrowheads indicate the LED location within each field of view, demonstrating consistent visual detection of air onset across cameras despite differences in perspective. **(B)** Binarized air-on state extracted independently from LED intensity signals in the paws

(magenta), face (cyan), and pupil (green) videos, plotted over the full recording session. Although small offsets in absolute timing are visible across modalities due to independent acquisition clocks, trial structure and air-on epochs are preserved across all streams. **(C)** Trial-by-trial comparison of air-on (left three panels) and air-off (right three panels) durations measured from LED-derived signals in each video modality versus the corresponding durations measured from the DAQ-recorded air-control signal (5 kHz; treated as ground truth). Each point represents a single trial, and diagonal lines indicate unity. Strong correspondence across modalities demonstrates that, despite minor onset/offset timing jitter, LED-based segmentation reliably captures air-on and air-off durations suitable for within-epoch behavioral and kinematic analyses.

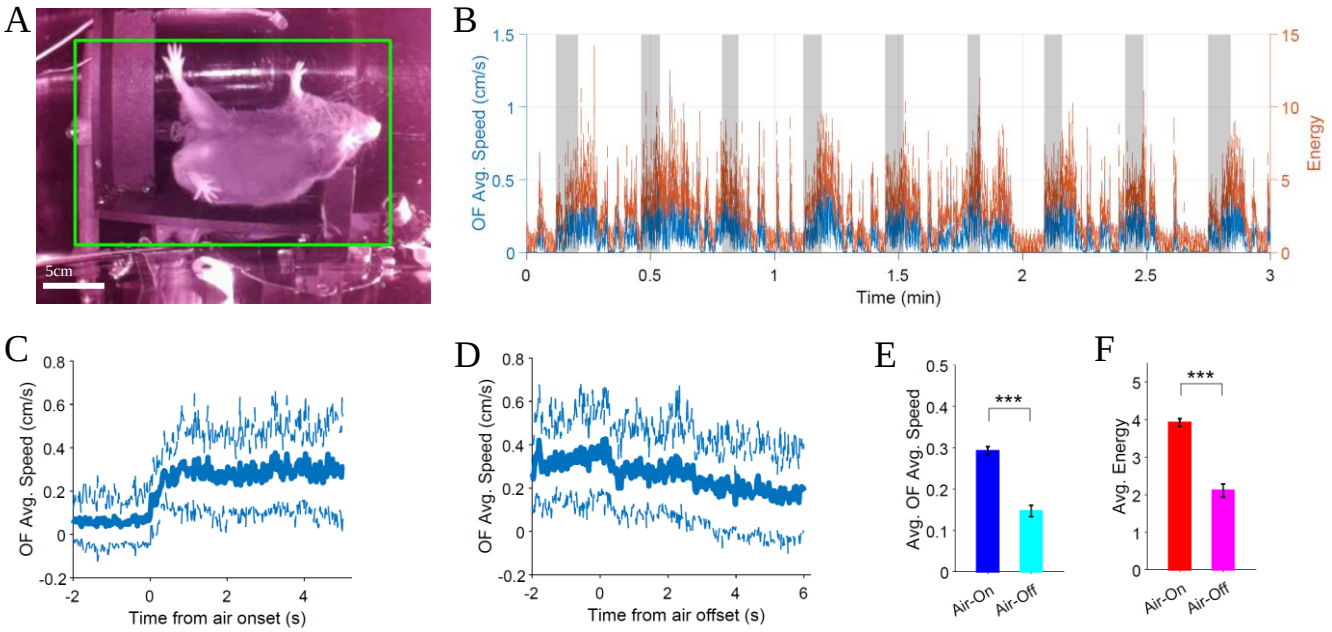

Figure 4. Whole-body kinematics during air-induced locomotion.

(A) Representative paw video frame showing the region of interest (ROI; green box) used for optical-flow (OF) and motion-energy extraction. Example tracked landmarks are overlaid to illustrate paw position within the ROI (scale bar, 5 cm). **(B)** Time series of paw optical-flow–derived average speed (blue, left axis) and motion energy (orange, right axis) over a representative recording segment. Shaded gray regions denote air-on epochs identified from the LED-based air signal. **(C)** Trial-averaged OF speed aligned to air onset (t = 0 s). Solid line indicates the mean across trials; dashed lines indicate ± SD. **(D)** Trial-averaged OF speed aligned to air offset (t = 0 s), plotted as in (C). **(E)** Mean paw OF speed during air-on versus air-off epochs, averaged across trials (n = 34). Bars show mean ± SEM; ***$p < 0.001$ (paired t-test). **(F)** Mean paw motion energy during air-on versus air-off epochs (n = 34), plotted as in (E).

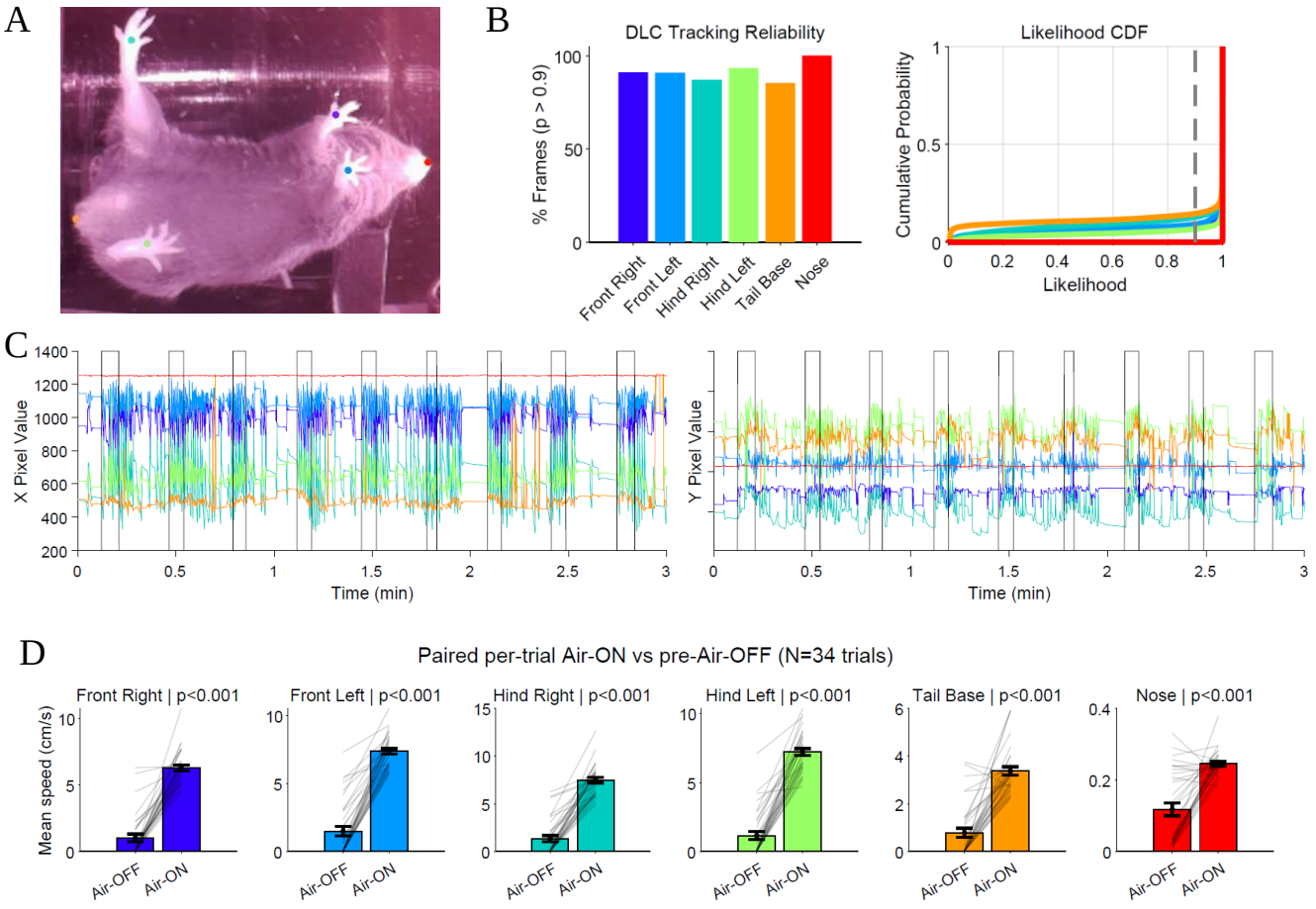

Figure 5. DeepLabCut-based paw and body kinematics during air-induced locomotion.

(A) Example frame from the paw-view video showing DeepLabCut tracking of forelimbs, hindlimbs, tail base, and nose. Colored markers indicate tracked body points used for kinematic analysis. **(B)** Tracking reliability across body parts. Left: percentage of frames with likelihood > 0.9 for each tracked point. Right: cumulative distribution functions (CDFs) of likelihood values, demonstrating consistently high confidence across body parts. **(C)** Horizontal (X; left) and vertical (Y; right) pixel trajectories of all tracked body points over time. Shaded regions indicate air-on epochs, illustrating structured, stimulus-locked changes in paw and body position during air-induced locomotion. **(D)** Trial-wise comparison of mean paw and body-point speed during air-on versus pre-air-off periods (N = 34 trials). Each gray line

represents a single trial (paired comparison), bars show mean ± SEM. All tracked body points exhibited significantly higher movement speeds during air-on epochs (paired t-tests, all $p < 0.001$).

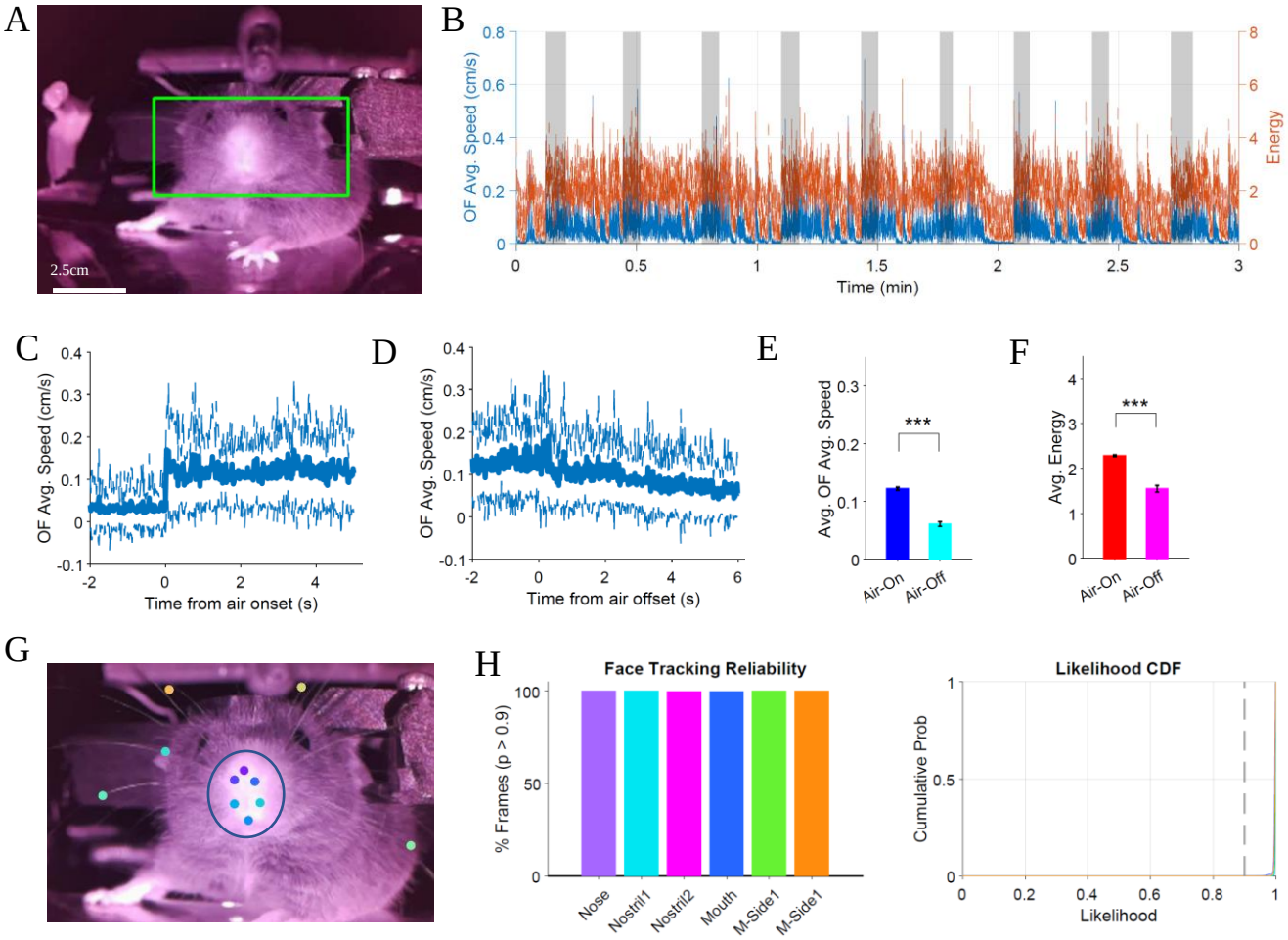

Figure 6. Front-facial kinematics during air-induced locomotion.

(A) Representative front-facial video frame illustrating the region of interest (ROI; green box) used for optical-flow (OF) and motion-energy extraction (scale bar, 2.5 cm). **(B)** Time series of OF-derived average facial motion speed (blue, left axis) and motion energy (orange, right axis) during a representative recording segment. Shaded gray regions indicate air-on epochs identified from the LED-based air signal. **(C)** Trial-averaged facial OF speed aligned to air onset (t = 0 s). Solid line indicates the mean across trials; dashed lines indicate ± SD. **(D)** Trial-averaged facial OF speed aligned to air offset (t = 0 s), plotted as in (C). **(E)** Mean facial OF speed during air-on versus air-off epochs, averaged across trials. Bars show mean ± SEM; ***p < 0.001 (paired t-test). **(F)** Mean facial motion energy during air-

on versus air-off epochs, plotted as in (E). **(G)** Example frame showing DeepLabCut-based tracking of front-facial landmarks (nose, nostrils, mouth, and snout-side points) used to assess tracking reliability. **(H)** DeepLabCut tracking performance across facial landmarks. Left: percentage of frames with likelihood > 0.9 for each tracked point. Right: cumulative distribution function (CDF) of likelihood values. Although whisker positions were included in the initial DeepLabCut model, whisker tracking was inconsistent under the present recording and analysis conditions and was not further optimized.

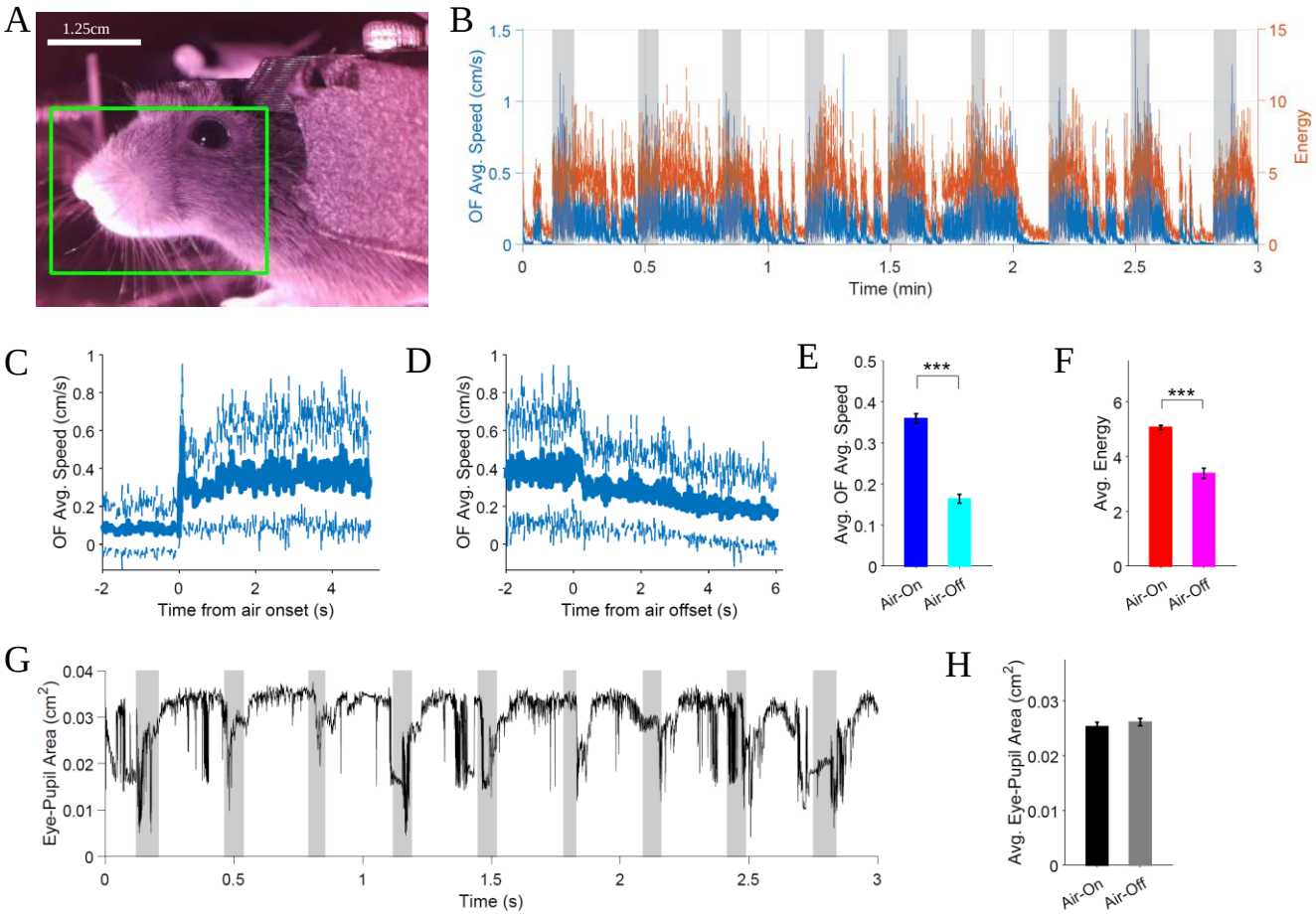

Figure 7. Side-facial and eye dynamics during air-induced locomotion.

(A) Representative side-facial video frame showing the region of interest (ROI; green box) used for optical-flow (OF) and motion-energy extraction from the facial and periocular region (scale bar, 1.25 cm). **(B)** Time series of OF-derived average facial motion speed (blue, left axis) and motion energy (orange, right axis) during a representative recording segment. Shaded gray regions indicate air-on epochs identified from the LED-based air signal. **(C)** Trial-averaged facial OF speed aligned to air onset (t = 0 s). Solid line denotes the mean across trials; dashed lines indicate ± SD. **(D)** Trial-averaged facial OF speed aligned to air offset (t = 0 s), plotted as in (C). **(E)** Mean facial OF speed during air-on versus air-off epochs, averaged across trials. Bars show mean ± SEM; ***$p < 0.001$ (paired t-test). **(F)** Mean facial motion energy during air-on versus air-off epochs, plotted as in (E). **(G)** Time series of eye-region

area extracted from side-facial video, illustrating stability of overall eye opening across air-on and air-off epochs. **(H)** Mean eye-region area during air-on versus air-off epochs, showing no significant difference between conditions. Experiments were conducted in darkness, resulting in a maximally dilated pupil. Consequently, no air-evoked modulation of pupil size was observed. The absence of systematic pupil-area changes confirms that the red LED used to signal air delivery did not induce measurable autonomic pupil responses under these recording conditions.

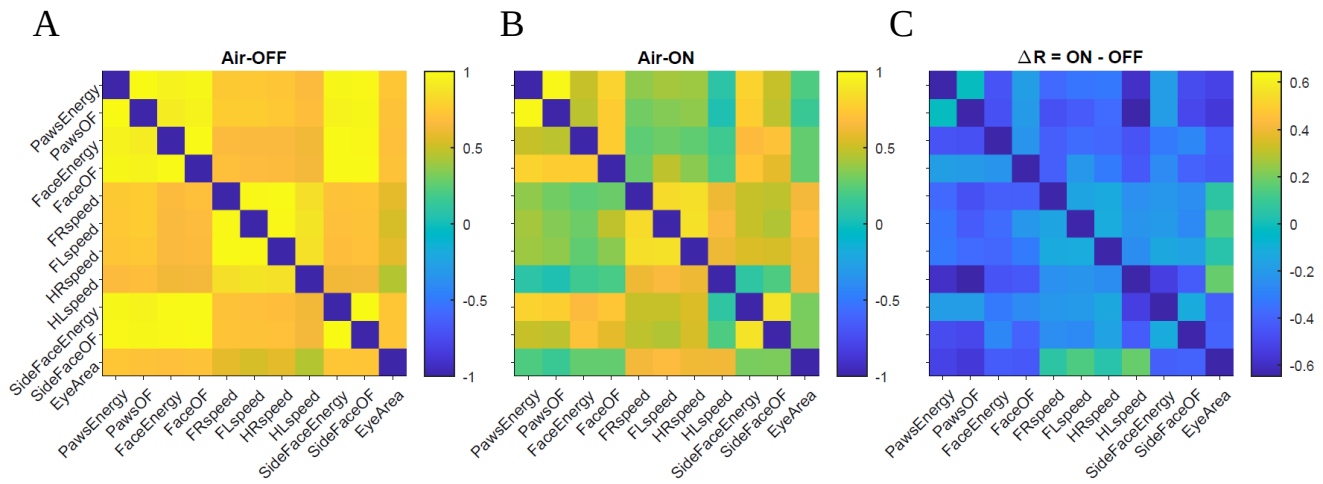

Figure 8. State-dependent reorganization of coordinated body kinematics.

(A) Trial-mean correlation matrix computed during air-off epochs across behavioral and kinematic measures (N = 34 trials). Measures include paw motion energy (PawsEnergy), paw optical-flow–derived speed (PawsOF), front-facial motion energy (FaceEnergy), front-facial optical-flow speed (FaceOF), individual paw speeds derived from DeepLabCut for front right (FRspeed), front left (FLspeed), hind right (HRspeed), and hind left (HLspeed), side-facial motion energy (SideFaceEnergy), side-facial optical-flow speed (SideFaceOF), and eye-region area (EyeArea). Diagonal elements (self-correlations) are masked to emphasize cross-modal relationships. **(B)** Corresponding trial-mean correlation matrix during air-on epochs. Air-on periods show a redistribution of correlations across limb, facial, and whole-body measures, consistent with a transition to a coordinated locomotor state. **(C)** Difference matrix (ΔR = air-on − air-off), illustrating state-dependent changes in inter-measure coupling. Positive values indicate increased coordination during air-on epochs, whereas negative values reflect reduced coupling relative to air-off. These results demonstrate that air-induced locomotion is accompanied by a structured reorganization of multi-modal kinematic relationships rather than a uniform increase in movement magnitude.